

Strong and Weak 3D Topological Insulators Probed by Surface Science Methods

Markus Morgenstern,* Christian Pauly, Jens Kellner, Marcus Liebmann, Marco Pratzner, Gustav Bihlmayer, Markus Eschbach, Lukacz Plucinski, Sebastian Otto, Bertold Rasche, Michael Ruck, Manuel Richter, Sven Just, Felix Lüpke, and Bert Voigtländer

The contributions of surface science methods to discover and improve 3D topological insulator materials are reviewed herein, illustrated with examples from the authors' own work. In particular, it is demonstrated that spin-polarized angular-resolved photoelectron spectroscopy is instrumental to evidence the spin-helical surface Dirac cone, to tune its Dirac point energy toward the Fermi level, and to discover novel types of topological insulators such as dual ones or switchable ones in phase change materials. Moreover, procedures are introduced to spatially map potential fluctuations by scanning tunneling spectroscopy and to identify topological edge states in weak topological insulators.

types of topologies in crystalline solids, mostly appearing without magnetic fields.^[6–8] The overwhelming success has also led to activities in other fields of physics enabling, e.g., the guiding of light or sound along arbitrarily shaped edges.^[9–12] The attractive robustness of the topological properties, tied to the integer character of the topological indices, implied a multitude of proposals also for electronic applications.^[13–15] This currently culminates in the actively pursued dream to realize topological quantum computation via parafermions.^[16–19] The central advantage of this

1. Introduction

Topology became a classification scheme for solid-state electronic properties in the 1980s while describing the robustness of the quantum Hall effect.^[1,2] This achievement has been honored most notably by the Noble prize 2016 for physics.^[3,4] The well-deserved appreciation was largely triggered by the experimental discovery of 2D topological insulators (2DTIs) in 2007.^[5] This discovery initiated a major effort in experimental and theoretical solid-state physics leading to a multitude of other


approach is the robustness of corresponding quantum operations against local perturbations as long as the quasiparticles remain in their topologically protected subspace.

From the materials science point of view, the intriguing observation that a lot of well-known materials are 3D strong topological insulators added a crucial view on electronic band structure properties.^[6–8] It turned out that a large amount of bulk insulators necessarily provide spin helical conductive surface states^[20–22] via the symmetry of their bulk band structure described by a topological index.^[23,24] The presence of such surface states is

Prof. M. Morgenstern, Dr. C. Pauly, Dr. J. Kellner, Dr. M. Liebmann, Dr. M. Pratzner
II. Institute of Physics B and JARA-FIT
RWTH Aachen University
52074 Aachen, Germany
E-mail: mmorgens@physik.rwth-aachen.de

Dr. G. Bihlmayer
Peter Grünberg Institut (PGI-1)
Institute for Advanced Simulation (IAS-1)
Forschungszentrum Jülich GmbH and JARA
52425 Jülich, Germany

Dr. M. Eschbach, Dr. L. Plucinski
Peter Grünberg Institut (PGI-6)
Forschungszentrum Jülich GmbH and JARA
52428 Jülich, Germany

 The ORCID identification number(s) for the author(s) of this article can be found under <https://doi.org/10.1002/pssb.202000060>.

© 2020 The Authors. Published by WILEY-VCH Verlag GmbH & Co. KGaA, Weinheim. This is an open access article under the terms of the Creative Commons Attribution License, which permits use, distribution and reproduction in any medium, provided the original work is properly cited.

DOI: 10.1002/pssb.202000060

Dr. S. Otto
Lehrstuhl für Festkörperphysik
Universität Erlangen-Nürnberg
91058 Erlangen, Germany

Dr. B. Rasche, Prof. M. Ruck
Faculty of Chemistry and Food Chemistry
TU Dresden
01062 Dresden, Germany

Dr. M. Richter
Leibniz Institute for Solid State and Materials Research
Dresden Center for Computational Science
IFW Dresden
P.O. box 270116, 01171 Dresden, Germany

S. Just, Dr. F. Lüpke, Prof. B. Voigtländer
Peter Grünberg Institut (PGI-3)
Forschungszentrum Jülich GmbH and JARA
52428 Jülich, Germany

totally independent on details of the confining surfaces and, moreover, these surface states are protected against backscattering by their spin helicity.^[6,25] Hence, such materials can be thought of as a third conductivity class in addition to conductors and insulators, being insulating in the interior of the system but conducting on its surfaces. Favorably, a simple classification scheme exists in case of inversion symmetry of the crystal.^[25] It simply multiplies the parities (point inversion symmetries) of occupied single-electron states at the time-reversal invariant momenta (TRIMs) of the Brillouin zone to deduce the topological index. This provides an easy tool to exploit the much more complex theoretical background, that relies on extracting topological indices from general symmetries of the describing Hamiltonian^[23,24,26–28] partly combined with crystal symmetries.^[29,30] High-throughput density functional theory (DFT) calculations can be used to automatically extract candidate topological insulators from the extensive data base existing for crystalline materials.^[20,21] This often leads to materials with large band gap such that the topological transport properties can be observed at room temperature.

However, subsequently, the candidate materials still have to be verified and characterized by experimental methods. This is due to the inherent minor difficulties of DFT calculations such as the missing precise description of electronic correlations and of van-der-Waals interactions^[31,32] as well as the typically too small bandgap. As surface states are the decisive fingerprint of 3D topological insulators (3DTIs), well-established surface science methods became the tool of choice for the task of confirmation. In particular, angular-resolved photoelectron spectroscopy (ARPES) directly maps the spin helical surface states in k space,^[33,34] that typically exhibit a Dirac-type linear dispersion around one of its TRIMs in the Brillouin zone.^[35] The spin-polarized version of ARPES (SARPES) moreover can characterize the spin-helical Dirac character of the topological surface states (TSSs).^[34] Both can be compared directly with DFT-based calculations enabling an immediate verification of the topology.^[6–8] Moreover, the doping level and, thus, the position of the intrinsic Fermi level E_F with respect to the Dirac point (DP) energy E_D can be checked via ARPES.^[36] This is decisive for any type of applications in electronic devices requiring the Dirac cone to be present at E_F .

For exploitations of topological insulators in electric transport experiments, it turned out that disorder is detrimental.^[37] First, point defects acting either as acceptors or donors can make the interior conductive by shifting E_F into bulk bands.^[38,39] Hence, the bulk conductivity often overwhelms the conductivity of the TSSs.^[40] Second, surface doping can lead to a surface band bending that hosts additional 2D states of nontopological origin at E_F , while the TSSs are detuned from E_F .^[41,42] The latter is difficult to avoid, as any contamination on the surface, resulting, e.g., from device preparation, can imply a band bending that even appears after a few minutes of ultraviolet (UV) illumination in ultrahigh vacuum (UHV).^[43] Finally, even in case that E_F is favorably positioned within the bulk bandgap, compensation doping can lead to such strong potential fluctuations that electron and hole puddles appear in the interior of the sample implying hopping transport that competes with the transport via the TSSs.^[44,45] Thus, experimental access to the potential disorder is crucial for improving the transport properties. The potential disorder can be mapped on small length scales by scanning tunneling



Markus Morgenstern is a professor of experimental physics at RWTH Aachen since 2004. He was involved in setting up the Jülich Aachen Research alliance (JARA) as scientific director and was speaker of the DFG research unit “Relaxation and coherence phenomena of electron spins”. He is now principal investigator in the EU flagship “Graphene” and in the DFG excellence cluster “Matter and light for quantum computing (ML4Q)”. His main scientific subject is nanoscale investigations of electronic properties by low-temperature scanning tunneling microscopy, e.g., on topological materials or exfoliated 2D materials. Moreover, he develops novel scanning probe methods.

spectroscopy (STS).^[46,47] Therefore, one either uses the spatial variation of features in the local density of states (LDOS) related to E_D or the band edges^[48–50] or, more precisely in energy, by spatially tracking Landau level energies in magnetic field B .^[39,51–54]

In addition, STS can map 1D topological states that are difficult to probe via ARPES,^[55,56] as these states are typically only sparsely dispersed on the surface. STS identifies the topological edge states straightforwardly as the increased intensity of the LDOS at step edges.^[57–63] Its distinctive property of prohibited backscattering appears via the missing standing waves. Such standing waves are very pronounced for conventional 1D electronic states due to the strongly confined 1D geometry.^[64] Hence, its absence is a strong fingerprint of prohibited backscattering. 1D topological edge states have been found for 2DTIs,^[57,63,65] weak topological insulators,^[58–60] and at step edges of topological crystalline insulators, where they are caused by a symmetry breaking of the crystal at these edges.^[61]

In this Short Review, we will exemplify the mentioned surface-science-based approaches to topology in crystals. These approaches are still central tools for the characterization of different topologies as well as for the finding of novel prospective materials within an established class of topology.^[66] For the sake of simplicity, we restrict illustrations to our own work that cover many of the central developments yet. We cannot review the literature extensively, already due to the bare amount, but concentrate on initial publications and central additional insights on methodology.

2. Identifying Topological Surface States

Soon after establishing 2DTIs experimentally^[5] based on theoretical predictions,^[26] an extension of the formalism to 3D was proposed.^[24,25] It results in two types of 3DTIs. One exhibits an odd number of spin-helical TSSs on each surface and is dubbed strong 3DTI, whereas the other one has an even number of TSSs on every surface except one and is dubbed weak 3DTI.^[24,25] After identifying a first strong 3DTI in a BiSb alloy by ARPES,^[33] DFT calculations predicted stoichiometric materials to be strong 3DTIs, namely Bi_2Te_3 , Sb_2Te_3 , and Bi_2Se_3 .^[35] These three materials share the same crystal structure of quintuple layers (QLs) that are stacked on each other by van-der-Waals forces

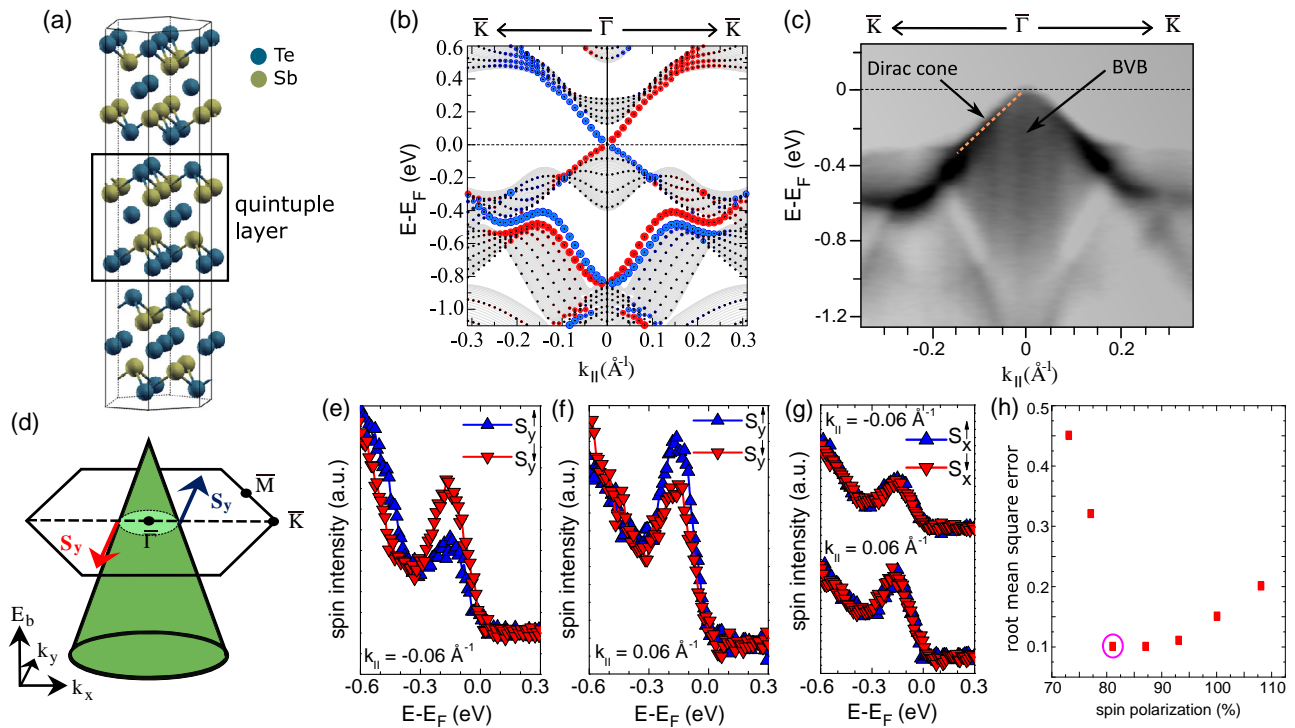


Figure 1. Identifying TSSs. a) Structural model of Sb_2Te_3 with marked QL. b) Band structure of Sb_2Te_3 in $\bar{K}\bar{\Gamma}\bar{K}$ direction, as calculated by DFT including spin–orbit coupling. States are shown as circles with colors (blue or red) that indicate different in-plane spin directions perpendicular to k_{\parallel} as resulting from a thin-film calculation. The size of the colored circles marks the magnitude of the spin density of the state near the surface. Shaded areas are projected bulk bands originating from a bulk calculation. The strongly spin-polarized states have been checked to be surface states. c) ARPES data of the lower Dirac cone of in situ-cleaved $\text{Sb}_2\text{Te}_3(0001)$ recorded along $\bar{K}\bar{\Gamma}\bar{K}$ (\bar{K} : high intensity, $\bar{\Gamma}$: low intensity). States from the BVB are marked. Orange, dashed line is a guide to the eye along the Dirac cone revealing a Dirac velocity $v_F = 3.8 \pm 0.2 \times 10^5 \text{ m s}^{-1}$, photon energy $h\nu = 55 \text{ eV}$. d) Sketch of the lower Dirac cone with spin directions s_y marked as deduced from DFT (b) and in accordance with SARPES (e–g). e, f) Spin-resolved energy distribution curves (EDCs) for the spin component perpendicular to k_{\parallel} at k_{\parallel} -values as indicated. Different colors mark different spin directions as in (b), $h\nu = 54.5 \text{ eV}$. g) Spin-resolved EDCs for the spin component parallel to k_{\parallel} , $h\nu = 54.5 \text{ eV}$. h) Root-mean-square error for the deduced spin polarization of the TSS according to the SARPES data of (e, f) after using fits to adequately subtract contributions from bulk bands, other surface bands, and inelastic scattering (for details see the study by Pauly et al.^[72]). Best fit value is encircled. $T = 300 \text{ K}$. Adapted with permission.^[72] Copyright 2010, American Physical Society.

(Figure 1a). Hence, these materials can be cleaved in situ and can be exfoliated as thin films.^[67,68] Moreover, they have been predicted to exhibit a single TSS on the cleavage plane with the DP located in the center of the Brillouin zone at the so-called $\bar{\Gamma}$ point (Figure 1b).^[35]

These properties enable a simple investigation by SARPES provided that the Dirac cone (TSS) is below E_F . Indeed, the first ARPES measurements of a TSS on $\text{Bi}_2\text{Se}_3(0001)$ have been published^[69] back to back with the DFT-based predictions.^[35] First SARPES measurements appeared only 3 months later.^[34] It turned out that the cleaved bulk samples of Bi_2Se_3 and Bi_2Te_3 are n-doped, being beneficial for the ARPES mapping of the TSS, but detrimental for electric transport. In contrast, Sb_2Te_3 is usually p-doped,^[70,71] impeding ARPES mapping. Fortunately, we obtained a 20 year-old Sb_2Te_3 crystal that enabled mapping of the lower part of the Dirac cone via ARPES (Figure 1c).^[72] This part of the Dirac cone encloses states of the bulk valence band (BVB) in k space in quantitative accordance with DFT calculations (Figure 1b). As the doping is caused by point defects of the material,^[73,74] we speculate that the particular defect distribution within this material is responsible for

establishing the favorable $E_D \approx E_F$. Similar results exhibiting Dirac cones within the bandgap close to E_F have also been found for Sb_2Te_3 , Bi_2Se_3 , and Bi_2Te_3 after careful optimization of growth conditions in UHV.^[49,73,75]

Figure 1e–g shows SARPES data recorded via a Mott detector, that probes the two in-plane directions of the spin. Two peaks at opposite k are recorded corresponding to the two opposite sides of the Dirac cone. The spin polarization is found to be exclusively perpendicular to the k vector as expected from the (Rashba-type) spin–orbit interaction. It is, moreover, helical, i.e., it switches sign when inverting k . These are the typical fingerprints of a Dirac cone type TSS.^[35] Out-of-plane spin polarizations have also been observed, in particular, further away from E_D and are traced back to distortions of the simple Dirac cone, e.g., via warping, i.e., by influences of the crystal structure.^[76] It is important to realize that SARPES does not probe the spin polarization of the initial state exclusively, but that the photoemission process is an excitation to unoccupied states extending into the vacuum that can change the spin polarization either by matrix effects or by spin polarization of the final state.^[77] This can be captured by calculations within the so-called fully relativistic one-step model based on

DFT calculations.^[78] In particular, at low photon energies, it turns out that the detected spin polarization can even be inverted with respect to the initial state depending on the polarization direction of the exciting light.^[79] At higher energies in the deep UV regime, this is less relevant, as excited states are well above the vacuum level. Hence, the helicity of the TSS can be deduced being counterclockwise for the lower part of the Dirac cone of Sb_2Te_3 (Figure 1d). This is in accordance with the DFT calculations (Figure 1b). The absolute value of the spin polarization of the TSS is not extracted directly from our SARPES data due to the limited angular and energy resolution. The reduced resolution during SARPES with respect to ARPES is caused by the low efficiency of the Mott detector. Novel approaches improve this efficiency considerably via spin dependent, k conserving reflections of the photoelectrons at single crystals.^[80] Hence, resolution can be much better, but such apparatus was not available during the measurements shown in Figure 1. Consequently, spin polarization had to be extracted rather indirectly by carefully subtracting the inelastic background, the background originating from the also measured spin-polarized surface states at lower energy (visible in Figure 1b at -0.4 to -0.8 eV), and the background from the overlapping, enclosed bulk states. Nevertheless, the accordingly best fit of the SARPES data revealed a spin polarization of the TSS of 80 – 95% (Figure 1g) matching the DFT result of 90% surprisingly well.^[72] Obviously, the TSS is not 100% spin polarized, albeit it is spin helical. This is a natural consequence of spin–orbit interaction, that strongly mixes the spin with orbital degrees of freedom via the heavy atoms involved. Thus, spin is not a good quantum number in these materials.

3. Tuning the Dirac Point Energy

One main task after the experimental discovery of 3DTIs was to tune their DP energy E_D , that mostly turned out to be far away from E_F .^[8] Hence, literally speaking, the first 3DTIs were not even insulators in their interior. More importantly, the transport properties of the 3DTIs could not be probed without rendering the bulk of the material sufficiently insulating. A rather obvious, initial approach was to exploit the opposite p-type doping of Sb_2Te_3 and n-type doping of Bi_2Te_3 or Bi_2Se_3 . Two main strategies have been pursued. Either, the two materials are mixed in a way such that they exhibit a similar density of acceptors and donors.^[81,82] This approach eventually led to the observation of the quantum Hall effect within thin films of BiSbTeSe_2 as a clear signature of dominating 2D-type transport.^[83,84] A detailed analysis of the filling factor dependence of the Hall conductance identified the TSSs on bottom and top surfaces as the origin of the half integer quantum Hall effect.^[84] The respective tuning of the Dirac cone, namely of E_D with respect to E_F , can be monitored by ARPES in detail.^[85] This is particularly important for the protection of Majorana states within vortices of a topological superconductor against conventional single-particle excitations by an effective gap $E_{\text{gap,eff}}$ reading^[86–88]

$$E_{\text{gap,eff}} \simeq \frac{\Delta^2}{\sqrt{\Delta^2 + (E_F - E_D)^2}} \quad (1)$$

with Δ being the excitation gap of the surrounding topological superconductor.

Figure 2a shows the results for $(\text{Bi}_{1-x_{\text{Sb}}}\text{Sb}_{x_{\text{Sb}}})_2\text{Te}_3$ at different mixing of Sb and Bi including the case of $E_F \simeq E_D$. Corresponding ARPES data at $x_{\text{Sb}} = 94\%$ are shown in Figure 2b.^[85,89] Figure 2c–f shows the evaluation of the data. The k_{\parallel} values of the TSS are obtained from fitting intensity profiles $I(k_{\parallel})$ (Figure 2c) at different energies that are subsequently extrapolated linearly to determine the crossing point as E_D (Figure 2d). Alternatively, the full width at half maximum (FWHM) of $I(k_{\parallel})$ closer to E_D (Figure 2e) is used via identifying E_D as the energy with lowest FWHM (Figure 2f). In both cases, E_F has to be carefully calibrated as well. For the particular sample, we found $E_F \simeq E_D$ within 5 meV.^[89] As no time-dependent band shifts were observed, the value is likely robust as long as the sample is in UHV. However, ex situ Hall measurements on identically prepared samples exhibit a transition from p-type to n-type bulk conduction at much lower Sb concentration ($x_{\text{Sb}} \simeq 60\%$).^[90] Hence, rescuing the precise tuning for electric devices requires additional efforts and investigations.

Another approach uses the electric field at interfaces between p-type and n-type 3DTIs.^[91,92] As well known for semiconductor p–n junctions, a depletion region forms at the interface such that a thin enough overlayer can maintain in the depletion region. This implies that E_F remains in the bandgap up to the surface. The approach has the general advantage that it avoids ternary or quaternary alloys that potentially induce additional scattering centers for electrons via alloying. Figure 3a shows a transmission electron microscope (TEM) image of a stack of n-type and p-type 3DTIs grown by molecular beam epitaxy (MBE). A relatively sharp interface is observed via the material contrast due to different atomic weights of Bi and Sb. Figure 3b shows ARPES data at different thicknesses of the upper p-type Sb_2Te_3 on n-type Bi_2Te_3 . Obviously, the Dirac cone is shifted downward in energy with decreasing Sb_2Te_3 thickness. To determine E_D including the thicknesses, where it is above E_F , DFT results of 6 QL Sb_2Te_3 are overlaid after rigidly shifting them to reproduce the ARPES data. It turned out that the best anchor point for shifting is the surface state at lower energy (Figure 1b at -0.4 to -0.8 eV). This state is vertically stronger confined to the surface area and, hence, is more intense in ARPES and less prone to the averaging by the vertical band bending^[72] (details in the study by Eschbach et al.^[91]). The resulting $E_D - E_F$ has been compared with the result of a 1D Poisson–Schrödinger model revealing reasonable agreement (Figure 3c). The model is based on the charge carrier densities of MBE grown films of Sb_2Te_3 and Bi_2Te_3 as determined by Hall measurements, while assuming the same density of dopants and charge carriers. An intermixing at the interface is additionally considered that is deduced from Auger electron spectroscopy depth profiling.^[91] Obviously, the depletion method via p–n junction is also able to tune $E_F \simeq E_D$ for a thickness of ≈ 20 QL Sb_2Te_3 on top of Bi_2Te_3 .

4. Materials with Particular Properties: Dual Topological Insulators and Phase Change Materials

4.1. Dual Topological Insulators

Another important application of ARPES is to confirm desired properties of novel topological materials. This includes

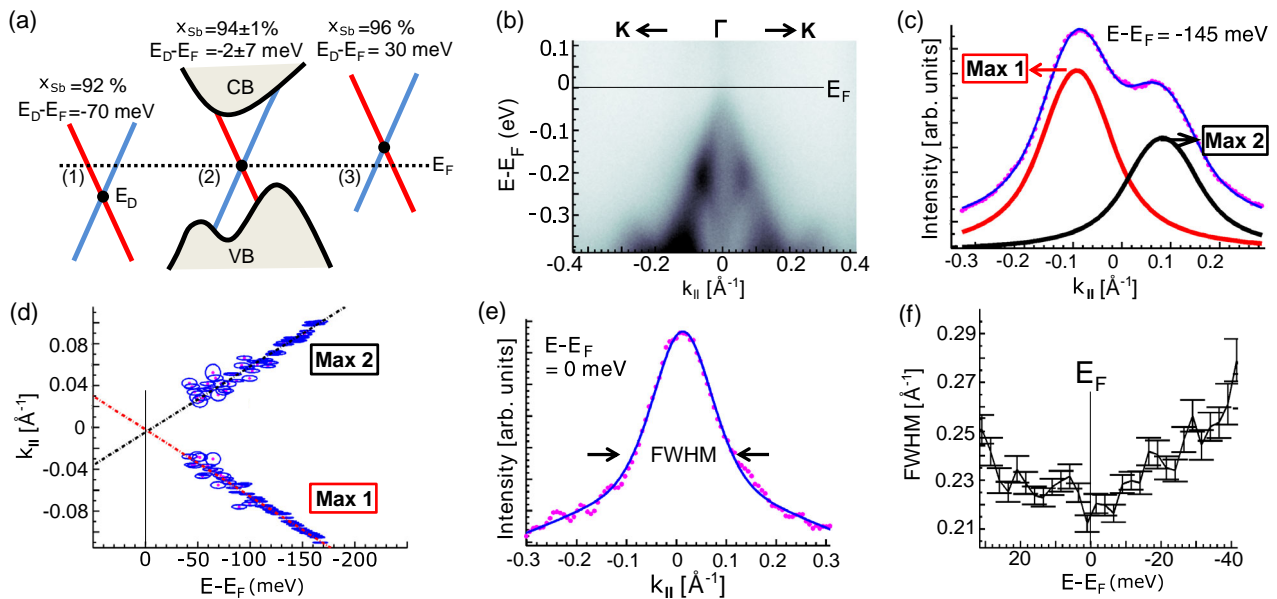


Figure 2. Tuning the DP by stoichiometry. a) Model of Dirac cone (blue, red lines) between the valence band (VB) and conduction band (CB) marked as gray areas for $(\text{Bi}_{1-x_{\text{Sb}}}\text{Sb}_{x_{\text{Sb}}})_2\text{Te}_3$ at different x_{Sb} . Resulting DP energy E_{D} with respect to E_{F} is indicated by the black dots. b) $E(k_{\parallel})$ dispersion along $\bar{K}\bar{\Gamma}\bar{K}$ (dark: high intensity, bright: low intensity) for $x_{\text{Sb}} = 94\%$, $h\nu = 21.2$ eV. Marked E_{F} is determined on polycrystalline Cu. c) Cut through (b) (pink dots) at $E - E_{\text{F}} = -145$ meV with fit curve (blue) consisting of two Voigt curves (black, red lines with indicated peak positions Max 1, Max 2). d) Energy-dependent peak positions (Max 1, Max 2) deduced from fits as shown exemplarily in (c) (red points with surrounding ellipses that enclose the 2σ confidence area). A linear regression of the data points (black, red dashed lines) is used to determine $E_{\text{D}} - E_{\text{F}} = -2 \pm 7$ meV. e) Cut through (b) at $E = E_{\text{F}}$ (pink dots) exhibiting only a single peak. One Voigt fit (blue) is used to deduce FWHM. f) FWHMs of single peaks as in (e), i.e., close to E_{F} . Error bars are marked. $T = 50$ K. Adapted with permission.^[89] Copyright 2015, AIP Publishing.

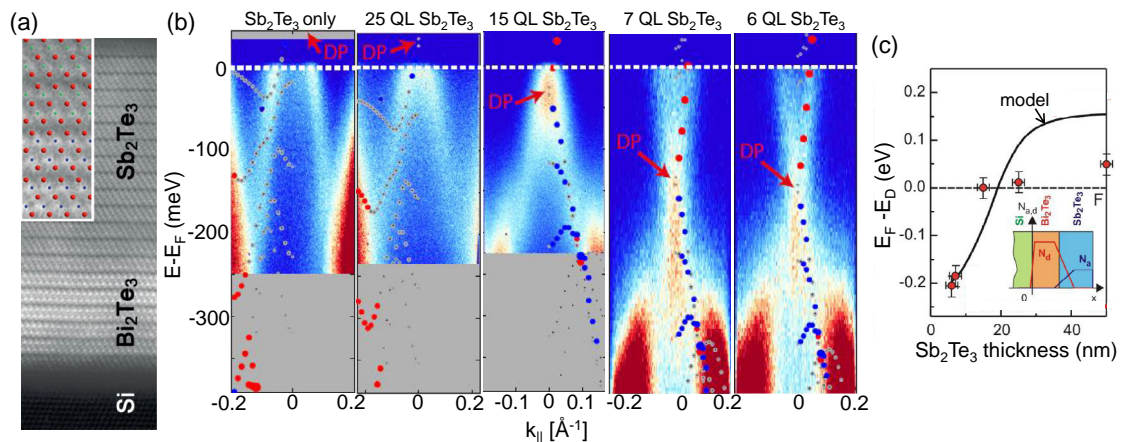


Figure 3. Tuning the DP by band bending. a) High-angle annular dark-field (HAADF) cross-sectional image recorded by TEM of $\text{Bi}_2\text{Te}_3/\text{Sb}_2\text{Te}_3$ stack grown by MBE on Si(111). Different brightnesses indicate chemical contrast via different atomic weights of Bi and Sb. Inset: zoom with overlaid symbols representing Te atoms (red), Sb atoms (green), and Bi atoms (blue), $T = 300$ K. b) ARPES data (blue–white–red color code) of different numbers of Sb_2Te_3 QDs (marked above) on top of $\text{Bi}_2\text{Te}_3/\text{Si}$, $h\nu = 8.4$ eV, $T = 15$ K. The first two (last three) data sets are recorded along $\bar{K}\bar{\Gamma}\bar{K}$ ($\bar{M}\bar{\Gamma}\bar{M}$). “ Sb_2Te_3 only” marks thick Sb_2Te_3 on Si without Bi_2Te_3 . DFT data of 6 QL Sb_2Te_3 (see also Figure 1b) are overlaid (symbols) after shifting in energy to optimally match experimental data. The resulting DP is marked. c) DP energies from ARPES (symbols) in comparison with a numerically solved 1D Poisson–Schrödinger model (full line). Inset: dopant densities used for the calculations as determined independently for both materials via Hall measurements (Bi_2Te_3 : n-type $N_{\text{D}} = 2 \times 10^{19} \text{ cm}^{-3}$, Sb_2Te_3 : p-type $N_{\text{A}} = 2 \times 10^{18} \text{ cm}^{-3}$). A linear interface intermixing across 5 nm is included as deduced from Auger electron spectroscopy depth profiling. Adapted under the terms of a Creative Commons Attribution 4.0 International License.^[91] Copyright 2015, Springer Nature.

topologically crystalline insulators (TCIs),^[93,94] Dirac semimetals^[95–97] and Weyl semimetals.^[98,99] Interestingly, the topological properties of different kinds can be combined in a single

material, if the topological indices belong to different symmetries of the Hamiltonian.^[100] For example, 3DTIs protected by time-reversal symmetry can be combined with TCIs protected by a

crystal symmetry such as n -fold rotation or mirroring.^[101] This raises the perspective to break one of the symmetries, hence, switching between different topology types.^[100,102] The first material that experimentally showed dual topology was Bi_1Te_1 .^[102] It consists of stacked Bi bilayers (BLs) and Bi_2Te_3 QLs in a ratio of 1:2 as evidenced by TEM (Figure 4a,b). Bi BLs are well known to be 2DTIs^[57,103,104] such that the stacking of such bilayers at sufficiently low interlayer interaction would result in a weak 3DTI. The so-called dark surface without TSS is simply the Bi BL surface, whereas the edge states of the BL lead to the TSSs at all other surfaces. The Bi_2Te_3 layers can be thought of as spacer layers between the Bi bilayers or as 2DTI layers themselves. Indeed, DFT calculations find a small bandgap of 0.1 eV around E_F for the intrinsic, i.e., undoped, Bi_1Te_1 with topological indices (0;001). This indicates a weak 3DTI with its dark surface perpendicular to the (001) direction.^[102] However, the reasoning via stacked 2DTIs is too simple, when analyzing the DFT data in more detail. Interlayer hybridizations mix up the 2D bands strongly, such that the weak 3DTI properties are rather accidental and not directly related to the 2DTI properties of the constituting layers. Intriguingly, the mirror Chern number of the same gap around E_F , that is protected by a mirror symmetry across the (1100) plane, is $n_M = -2$ rendering the system a TCI as well. Consequently, one expects an additional pair of Dirac cones on the dark (001) surface of the weak 3DTI Bi_1Te_1 . The DPs of these Dirac cones are necessarily located on the line in k space where the (001) surface intersects with the (1100) mirror plane. It must, moreover, be offset in opposite directions from $\bar{\Gamma}$. Figure 4c (upper row) shows a set of ARPES data in $E(k_{\parallel,1})$ representation that are recorded perpendicular to this mirror line for increasing $k_{\parallel,2}$ values along the line. The data exhibit an apparent Dirac cone as crossing of two bands at $k_{\parallel,2} \simeq 0.18 \text{ \AA}^{-1}$ and $E - E_F \simeq -0.2 \text{ eV}$. The development of the bands with $k_{\parallel,2}$ toward the crossing agrees nicely with

corresponding DFT results of $\text{Bi}_1\text{Te}_1(001)$ (Figure 4c, lower row). To achieve this agreement, the Bi_1Te_1 film had to be terminated by a single QL and had to be downshifted by 100 meV with respect to E_F . Both is reasonable with the latter accounting for n-type doping as expected from the well-known n-type doping of Bi_2Te_3 . The good agreement between ARPES and DFT data, also found for multiple other bands of Bi_1Te_1 , is the central evidence for the dual topological character of Bi_1Te_1 .^[102]

4.2. Topological Phase Change Materials

Another interesting class of 3DTI materials are commercially used in electronic applications. They are called phase change materials (PCMs) providing two favorable properties for data storage. First, they are fastly switchable (ns-scale) between the amorphous and a metastable crystalline phase at low energy penalty.^[105,106] Second, they exhibit a strong difference in optical reflectivity and electric conductivity between the two phases.^[107] Consequently, they are used in digital video disks (DVDs) and random-access memories.^[107] A standard class of PCMs is found on the pseudobinary line between the strong 3DTI Sb_2Te_3 and GeTe .^[108] The later material is also strongly influenced by spin-orbit interaction, revealing a strongly Rashba-split surface state and a strongly Rashba-split bulk state at E_F .^[109–111] Hence, it is natural to assume that some of the PCMs are 3DTIs as well. Indeed, DFT predicts 3DTI properties^[112–115] and finds that the 3DTI character depends strongly on details of the atomic arrangement.^[114,115] Figure 5a shows the structure of the most commonly used PCM $\text{Ge}_2\text{Sb}_2\text{Te}_5$ in its metastable phase. It consists of alternating layers of hexagonal Te and a mixture of Ge, Sb and vacancies. Whether these layers, stacked in ABC-type fashion, exhibit additional order in the Ge/Sb/vacancy layers or not depends on details of the preparation and is decisive for the 3DTI properties

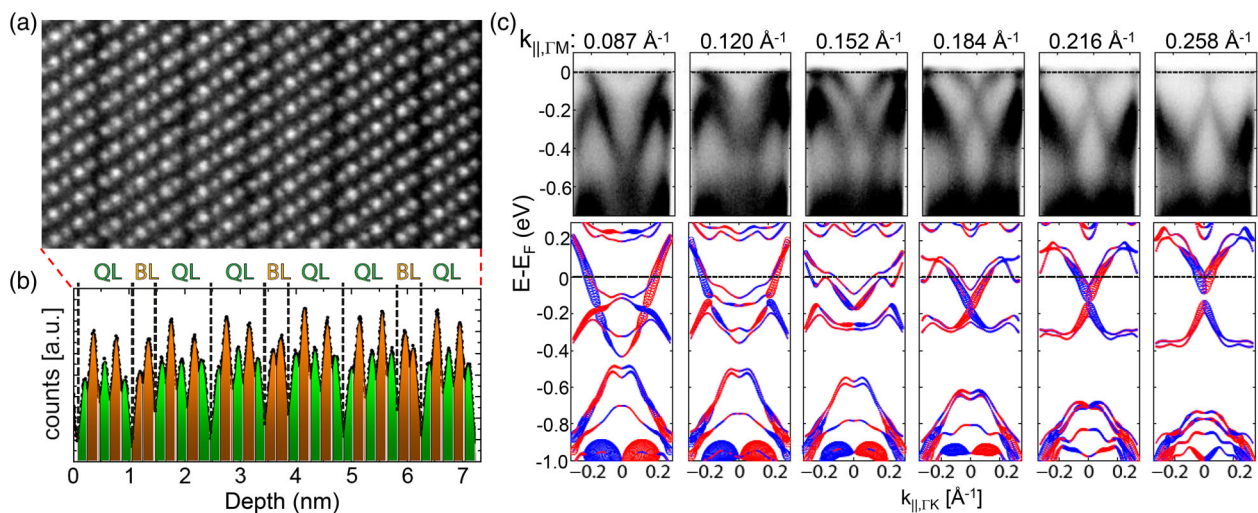


Figure 4. Dual topological insulator. a) Cross-sectional scanning TEM image zoomed into a 39 nm-thick Bi_1Te_1 on Si(111) and exhibiting atomic contrast caused by different atomic weights. b) Intensity profile line of (a) along the horizontal direction after averaging along the vertical direction. Deduced Bi (Te) layers are colored yellow (green). Bi_2Te_3 QLs and Bi bilayers (BL) are marked. c) Upper row: ARPES data parallel to $\bar{K}\bar{\Gamma}\bar{K}$ (dark: high intensity, bright: low intensity) for different k_{\parallel} along $\bar{\Gamma}\bar{M}$ as marked on top, $h\nu = 8.4 \text{ eV}$. Lower row: Corresponding band structure from DFT for a slab of 24 layers terminated by a single Bi_2Te_3 layer. Colors mark in-plane spin directions perpendicular to k_{\parallel} with spin polarization encoded as size of the circle. Adapted under the terms of a Creative Commons Attribution 4.0 International License.^[102] Copyright 2017, The Authors, published by Springer Nature.

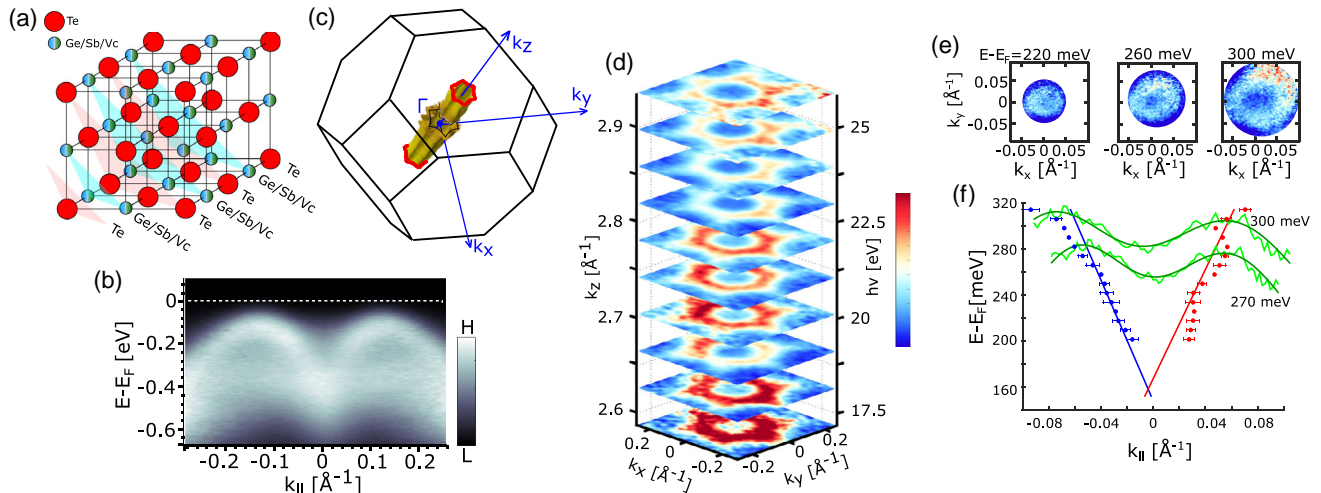


Figure 5. Topological PCMs. a) Structural model of the metastable rocksalt structure of $\text{Ge}_2\text{Sb}_2\text{Te}_5$ with intermixed layers of Ge, Sb, and vacancies (Ge/Sb/Vc). Adjacent (111) layers are highlighted by alternately colored, transparent triangles (pink, cyan). b) ARPES data along $\bar{K}\bar{\Gamma}\bar{K}$, $h\nu = 22.5$ eV. c) Brillouin zone of rock-salt $\text{Ge}_2\text{Sb}_2\text{Te}_5$ with principal \mathbf{k} directions marked including the measured so-called pseudo-Fermi surface (text) in gold. Resulting Fermi lines at the (111) side planes are drawn in red. d) ARPES intensity across (k_x, k_y) plane at E_F recorded for different $h\nu$ as marked. The corresponding k_z is calculated using an inner potential $E_{\text{inner}} = 14$ eV as deduced from the symmetry of the ARPES data along k_z (details in the study by Kellner et al.^[119]). e) Two-photon ARPES intensity $I(k_x, k_y)$ for different $E - E_F$ above E_F , i.e., within the unoccupied area of the bandgap, pump $h\nu = 1.63$ eV, probe $h\nu = 4.89$ eV, time delay $\Delta t = 1.33$ ps. (f) Green lines: cuts through (e) along k_y at $k_x = 0 \text{ \AA}^{-1}$ (jagged lines) with fits consisting of two Voigt peaks (smooth lines). Red, blue dots: peak positions of corresponding Voigt fits for several energies after averaging the cuts along two perpendicular \mathbf{k} directions. Red, blue lines: linear fits to the red and blue dots indicating a DP at $E_D - E_F = 160$ meV. Adapted under the terms of a Creative Commons Attribution 4.0 International License.^[119] Copyright 2018, The Authors, published by Springer Nature.

according to DFT.^[112–115] Hence, a subtle borderline between strong 3DTI and trivial properties appears. Based on these findings, it has been speculated that the reversible, strong difference in electric conductivity of a superlattice $\text{GeTe}/\text{Sb}_2\text{Te}_3$, that appears after applying voltage pulses without making the material amorphous, is caused by a switch in topology.^[116,117]

However, the experimental confirmation of strong 3DTI properties in PCMs is complicated by the p-type doping. Hence, initially the only evidence by ARPES was the M-shaped valence band with maxima away from $\bar{\Gamma}$ (Figure 5b)^[118] This configuration has been found in DFT calculations only for inverted bands representing a strong 3DTI.^[112–115] The p-type character of these bands is unconventional, as the energetically highest peak position in $I(E)$ plots is about 100 meV below E_F (Figure 5b). The p-type doping is instead realized by the tails of the disorder broadened valence bands that cut E_F . Hence, the ARPES intensity at E_F provides a k distribution mimicking the highest energy peaks below E_F (Figure 5c,d). This is called the pseudo-Fermi surface that can indeed be used to deduce the charge carrier density in good agreement with Hall measurements, if adequately weighted by the broadening of the valence bands due to disorder.^[119] Hence, disorder in the Ge/Sb/vacancy layer is the central ingredient for the conductivity of the metastable PCM phase.^[119]

The TSS above the broadened valence bands has been found by two-photon ARPES, i.e., a first light pulse transfers electrons into the initially unoccupied TSS and a second light pulse with time delay Δt extracts photoelectrons from the now-occupied TSS. Figure 5e shows data for several energies above E_F exhibiting a rather isotropic circle in \mathbf{k} space. The circle shrinks in diameter with decreasing energy. Extrapolation of the radius to lower

energies (Figure 5f) implies vanishing diameter at about 160 meV above E_F that represents E_D . Hence, the well-established conducting phase of the PCM $\text{Ge}_2\text{Sb}_2\text{Te}_5$ is a strong 3DTI, at least, after the preparation by MBE as probed in this study.^[119] This is appealing for 3DTI-based applications via exploiting the established expertise for upscaling conventional $\text{Ge}_2\text{Sb}_2\text{Te}_5$ devices.^[120] Counteracting the unfavorable p-doping of $\text{Ge}_2\text{Sb}_2\text{Te}_5$ is possible by the replacement of Ge with the heavier Sn,^[121] where, however, 3DTI properties still have to be demonstrated experimentally.^[122]

5. Disorder Characterization

As described in Section 1, a central task for improving the electric transport properties of 3DTIs (and 2DTIs) is the reduction of disorder. Disorder can lead to additional transport channels concealing the features of the TSS as well as to scattering of the TSS electrons.^[8,37] STS is the tool of choice for probing the disorder at the surface due to its unprecedented spatial and energy resolution in probing the LDOS. It has only the minor drawback that it is exclusively measuring the surface disorder, but not the disorder within deeper layers of the bulk of the crystal.^[123]

One possibility by STS is to track characteristic features of the energy-dependent LDOS.^[48,49] One measures $dI/dV(V)$ curves with I being the tunnel current and V being the voltage applied between tip and sample. Mostly, such curves are measured by lock-in technique, i.e., the tip-surface distance is stabilized at voltage V_{stab} and current I_{stab} . Afterward, the feedback loop is switched off, such that the tip surface distance remains constant, while the voltage is changed linearly and overlapped with an oscillating voltage of amplitude V_{mod} that enables the phase

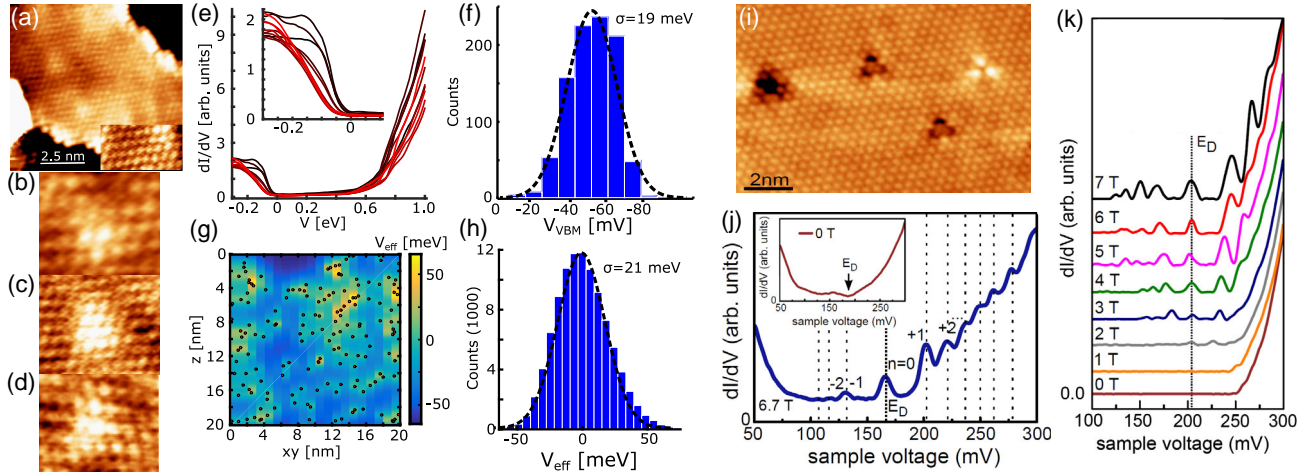


Figure 6. Mapping the disorder potential. a) STM image of in situ-transferred $\text{Ge}_2\text{Sb}_2\text{Te}_5(111)$ grown by MBE on $\text{Si}(111)$. The hexagonal atomic structure of the top Te layer is visible with inset at larger magnification, $V = -0.5$ V, $I = 100$ pA, $T = 300$ K. b–d) STM images of characteristic triangular protrusions indicating subsurface defects, $V = -0.5$ V, $I = 100$ pA, $T = 300$ K. e) Scaled $dI/dV(V)$ curves recorded at adjacent locations and displayed in different colors, $V_{\text{stab}} = -300$ mV, $I_{\text{stab}} = 50$ pA, $V_{\text{mod}} = 5$ mV, $T = 9$ K. Inset: zoom into the region of the valence band maximum (VBM). f) Histogram of VB onsets V_{VBM} as deduced from the peak energies in $d^3I/dV^3(V)$ curves (blue bars). A dashed Gaussian fit with marked σ width is added. g) Vertical cut through the simulated electrostatic potential $V_{\text{eff}}(x, y, z)$ for randomly distributed bulk acceptors (red dots) at density $N_A = 3 \times 10^{26} \text{ m}^{-3}$ as deduced from Hall measurements. h) Histogram of the potential values $V_{\text{eff}}(x, y)$ at the surface resulting from multiple simulations as in (g) (blue bars). A dashed Gaussian fit with marked σ width is added. i) STM image of in situ-cleaved $\text{Sb}_2\text{Te}_3(0001)$ exhibiting the hexagonally arranged top Te layer with clover-shaped defects likely Sb_{Te} (bright) and subsurface Vac_{Sb} (dark), $V = 0.4$ V, $I = 1$ nA, $T = 6$ K. j) $dI/dV(V)$ at $B = 6.7$ T showing Landau levels of the TSS marked by level index n at the dashed lines that result from Lorentzian fits of the peaks, $V_{\text{stab}} = 0.3$ V, $I_{\text{stab}} = 400$ pA, $V_{\text{mod}} = 4$ mV, $T = 6$ K. E_D is located at Landau level $n = 0$. Inset: $dI/dV(V)$ at $B = 0$ T (same position) with E_D marking the minimum of the curve, $V_{\text{stab}} = 0.3$ V, $I_{\text{stab}} = 50$ pA, $V_{\text{mod}} = 4$ mV, $T = 6$ K. k) $dI/dV(V)$ at $B = 0 - 7$ T as marked recorded on a different sample area as (j) and offset vertically, $V_{\text{stab}} = 0.3$ V, $I_{\text{stab}} = 100$ pA, $V_{\text{mod}} = 2$ mV, $T = 6$ K. The vertical dotted line indicates Landau level $n = 0$, hence, E_D . a–h) $\text{Ge}_2\text{Sb}_2\text{Te}_5$. Adapted with permission.^[50] Copyright 2017, American Physical Society. i–k) Sb_2Te_3 . Adapted with permission.^[54] Copyright 2015, American Physical Society.

sensitive detection of dI/dV via a lock-in amplifier. In first order, the resulting $dI/dV(V)$ represents the LDOS($E - E_F$).^[124–126] This gives direct access, e.g., to spatial variations of the bandgap for a semiconductor or insulator.

Figure 6a shows the (111) surface of the strong 3DTI $\text{Ge}_2\text{Sb}_2\text{Te}_5$ exhibiting Te as the top layer with hexagonal atomic structure.^[50] Several large triangular bright protrusions appear on top of the atomic lattice (Figure 6b–d). They have been identified as subsurface defects by comparison with DFT data.^[50] The lateral size of the triangle increases with the depth of the defect below the surface. The particular sample grown by MBE exhibits a defect density of $\approx 1.5 \times 10^{12} \text{ cm}^{-2}$. This implies a potential disorder due to the positive charging of most of the defects, in particular, vacancies.^[50,118,127] The $dI/dV(V)$ curves (Figure 6e) show a bandgap of about 0.5 eV with the valence band onset being close to E_F in agreement with optical absorption^[128] and ARPES data (Figure 5b), respectively. The bandgap onset is spatially varying. It is quantified via the peak position of the numerically determined $dI^3/dV^3(V)$ curves leading to a nearly Gaussian distribution of the spatially varying valence band onset with σ width of 20 meV (Figure 6f). We compare this with a simple model calculation randomly distributing positive point charges with a density identical to the charge carrier density determined by Hall measurements (Figure 6g). This leads to potential fluctuations on the surface with the same σ width as in the experiment (Figure 6h). It implies that the Coulomb

centers of the charged acceptors (vacancies) dominate disorder in this sample. Interestingly, the LDOS does not vanish within the bandgap (Figure 6e), indicating the presence of in-gap surface states in agreement with the two-photon ARPES revealing a TSS (Figure 5f).

Another possibility to map potential disorder is Landau level spectroscopy, however, requiring a magnetic field. It exploits the Dirac-type spin chirality of the TSS, implying a so-called zeroth Landau level (LL0) that is tied to E_D .^[129,130] Hence, tracking LL0 across the surface maps the potential disorder as seen by the TSS, i.e., averaged across some of the upper QIs.^[52–54] The lateral spatial resolution of the method is largely given by the magnetic length.^[131] Figure 6i shows STM data of in situ-cleaved $\text{Sb}_2\text{Te}_3(0001)$ featuring few defects that have been identified previously by comparison with DFT calculations as Sb substitutional in the upper Te layer (Sb_{Te} , bright) and vacancies in the Sb layer directly below the surface (Vac_{Sb} , dark).^[74] We find a defect density of $4 \times 10^{12} \text{ cm}^{-2}$ with all apparent defects attributed to the upper QL.^[54] Figure 6j,k shows Landau level spectra recorded at two different locations of the sample. It is apparent that the energy of LL0 does not shift with B field (Figure 6k). Moreover, LL0 appears at the same energy as the minimum in $dI/dV(V)$ curves at $B = 0$ T. Finally, LL0 deviates by ≈ 40 meV between the two probed areas, indicating the potential fluctuations. We found that the deduced LL0 energy correlates with the local density of defects visible in the STM data (not shown).^[54]

6. Edge States of Weak Topological Insulators

Weak 3DTIs have initially barely been studied due to the wrong conjecture that they are unstable with respect to most type of perturbations.^[25] More detailed studies, however, revealed that the only detrimental perturbation is a strong dimerization of adjacent layers along the surface normal of the dark surface leading to a doubling of the unit cell.^[132,133] Hence, also weak 3DTIs typically exhibit robust spin-helical surface states protected from backscattering. The most simple way to construct a weak 3DTI is stacking 2DTIs without interlayer interaction.^[25,133] This naturally implies that single-layer terraces on the dark surface are patches of 2DTIs that consequently must host 1D topological edge states at its step edges. These edge states are spin helical and, hence, ideal conductors as long as time-reversal symmetry is not broken.^[134] It turns out that such edge states appear generally for weak 3DTIs even if constructed differently.^[134] This implies the possibility to scratch a network of ideal conductors into the surface of a weak 3DTI.^[58]

The first experimental realization of a weak 3DTI was $\text{Bi}_{14}\text{Rh}_3\text{I}_9$.^[135] It consists of alternating layers of the 2DTI $(\text{Bi}_4\text{Rh})_3\text{I}$ ^[136] and the trivial insulator Bi_2I_8 (Figure 7a). The 2DTI exhibits a honeycomb unit cell such as graphene, but is made of the heavy atoms Bi, I, and Rh (Figure 7b). It, thus, mimics the initial idea of a 2DTI in a honeycomb lattice,^[26] but provides a much stronger spin-orbit interaction (≈ 1 eV) leading to a sizable inverted bandgap of 200–300 meV.^[136] This gap is much larger than in graphene with inverted bandgap of ≈ 20 μeV .^[137] Hence, the idea to construct the 3D material is to stack 2DTI honeycomb structures^[26] that are separated by trivial insulators as spacers impeding interactions between the 2DTI layers. However, it turned out that the strong spin-orbit interaction shifts much more bands across E_F than only the initial Dirac

cone of the honeycomb lattice that appears at E_F without spin-orbit interaction.^[130] Thus, the topological indices of a weak 3DTI again appear rather accidentally via inversion of several bands at the TRIMs of the Brillouin zone.^[136] Nevertheless, topological edge states at each step edge are expected and have been found by STS. They are directly visible as enhanced LDOS intensity at step edges (Figure 7c, background). In $dI/dV(V)$ curves, the bandgap region of the material (-0.15 to -0.35 eV) exhibits strong intensity exclusively at the step edges (Figure 7d). The edge states appear continuously along all edges^[58] and are only ≈ 1 nm wide perpendicular to the edge (Figure 7e). Moreover, the edge states did not exhibit any fingerprints of standing waves, but only intensity modulations periodic with the unit cell as expected for Bloch states. Thus, backscattering is largely impeded. Networks of topological edge states can indeed be scratched into the surface either by the tip of an atomic force microscope (AFM) (Figure 7f) with separation down to 25 nm^[58] or by the tip of an STM. The resulting scratches indeed show an increased LDOS within the bandgap (Figure 7g), but not at energies outside the gap (Figure 7h).

Unfortunately, E_F is not within the bandgap and, thus, the edge states are not accessible by electric transport. Nevertheless, four-tip STM measurements in UHV (Figure 8a)^[138] have been applied. They revealed that the resistance as a function of distance between the tips is not described by a 3D transport model only, but required a sizable contribution from a parallel 2D transport channel (Figure 8b,c). The best fit of the experimental data (red curve in Figure 8c^[139,140]) implies conductances for the 2D and 3D contributions, $\sigma_{2D} = 0.064 \pm 0.005$ S and $\sigma_{3D} = 9200 \pm 800$ S/m, respectively. Thus, the 2D conductance corresponds to a ≈ 7 μm -thick layer with the 3D conductance σ_{3D} .

This implies that the surface region of $\text{Bi}_{14}\text{Rh}_3\text{I}_9$ is significantly more conductive than the bulk. The encouraging finding

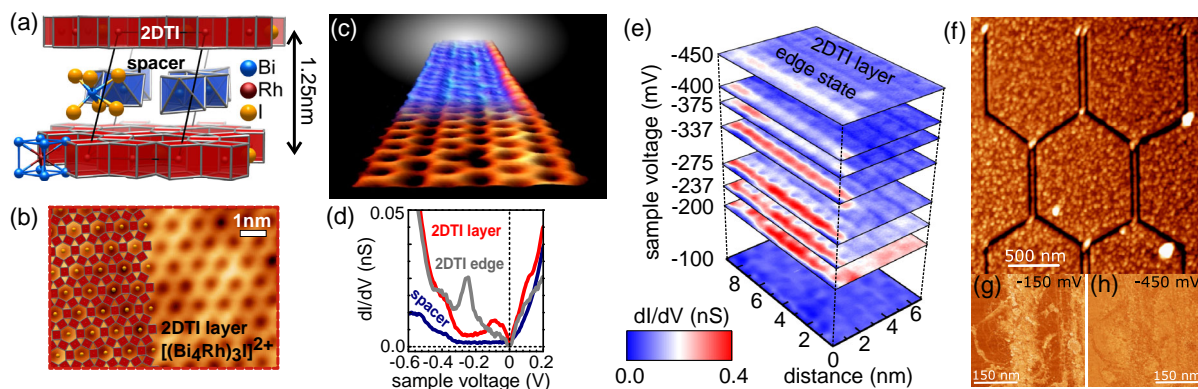


Figure 7. Edge states on the dark side of a weak topological insulator. a) Atomic model of $\text{Bi}_{14}\text{Rh}_3\text{I}_9$ consisting of alternating layers of the 2D topological insulator $(\text{Bi}_4\text{Rh})_3\text{I}$ (red) and the trivial insulator Bi_2I_8 (blue). b) STM image recorded on a $(\text{Bi}_4\text{Rh})_3\text{I}$ terrace with atomic model structure overlaid using the same color code as in (b), $V = 1.5$ V, $I = 100$ pA. c) 3D perspective of adjacent STM image (front area, $V = 0.8$ V, $I = 100$ pA) and dI/dV image (background, $V = -0.337$ V, $I = 100$ pA, $V_{\text{mod}} = 4$ mV), both recorded at the same $(\text{Bi}_4\text{Rh})_3\text{I}$ terrace confined by a step edge on the right. d) $dI/dV(V)$ recorded at a step edge of the $(\text{Bi}_4\text{Rh})_3\text{I}$ layer (grey), on a $(\text{Bi}_4\text{Rh})_3\text{I}$ terrace (red), and on a Bi_2I_8 terrace (blue), $V_{\text{stab}} = 0.8$ V, $I_{\text{stab}} = 100$ pA, $V_{\text{mod}} = 4$ mV. Notice the linearly vanishing dI/dV intensity around E_F caused by an Efros–Shklovskii-type Coulomb gap.^[151] e) Stacked dI/dV images recorded at the step edge of a $(\text{Bi}_4\text{Rh})_3\text{I}$ terrace for different V across the bandgap as marked on the left, $I_{\text{stab}} = 100$ pA, $V_{\text{mod}} = 4$ mV. f) Tapping-mode AFM image of $\text{Bi}_{14}\text{Rh}_3\text{I}_9$ after scratching a network of step edges into the surface by a carbon-coated Si cantilever at force $F = 1$ μN , $f_{\text{res}} = 275$ kHz, $k = 43$ N m^{-1} , $A = 30$ nm, set point: 70% (details see the study by Pauly et al.^[58]). g, h) dI/dV images of a scratch accomplished by one STM tip within UHV and afterward recorded by another tip at V as marked, $I = 300$ pA, $V_{\text{mod}} = 20$ mV. a–f) $T = 6$ K; g, h) $T = 300$ K. Parts (a,b,d,e,f) adapted with permission.^[58] Copyright 2015, Springer Nature.

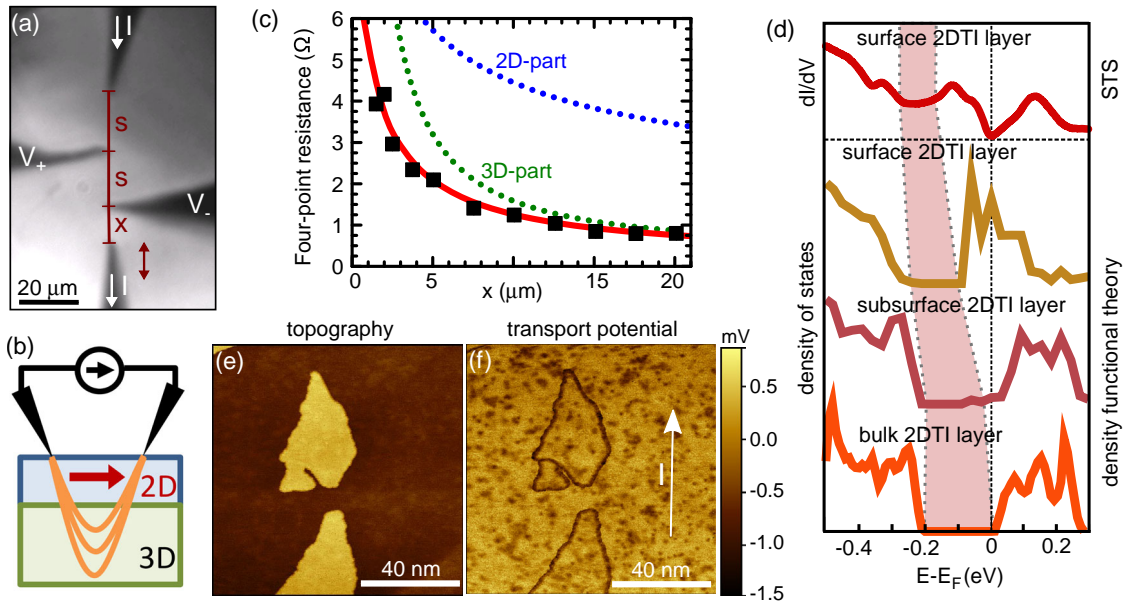


Figure 8. In situ electric transport of weak topological insulator $\text{Bi}_4\text{Rh}_3\text{I}_9$. a) Optical microscope image of the four tips positioned on $\text{Bi}_4\text{Rh}_3\text{I}_9$ within UHV. While the distances $s = 20 \mu\text{m}$ are kept constant during the four-point resistance measurements, x is changed. Applied current I and measured voltages V_+ and V_- are marked. b) Sketch of the two parallel transport paths (2D, 3D) used for the simulations of the four-point resistance in (c). c) Measured resistance $R = \frac{V_+ - V_-}{I}$ as function of x (black squares), $I = 0\text{--}300 \mu\text{A}$ used to extract the resistance from the resulting linear $V(I)$ curve, 300 K. A fit curve (red) is added consisting of the conductance of a 3D bulk contribution (green) and a 2D-type contribution (blue).^[139,152] d) Top curve: $dI/dV(V)$ recorded on a 2DTI layer ($(\text{Bi}_4\text{Rh})_3\text{I}$), $V_{\text{stab}} = 1 \text{ V}$, $I_{\text{stab}} = 70 \text{ pA}$, $V_{\text{mod}} = 4 \text{ mV}$. Two middle curves: layer resolved density of states of the surface and the inner 2DTI layer as deduced from a DFT calculation (FPLO code^[153]) of a slab with alternately stacked two 2DTI layers and two spacer layers (Bi_2I_8). Bottom curve: layer resolved density of states of the 2DTI layer deduced from a DFT calculation of an infinitely extended bulk crystal. Gap areas are marked in pink for all four curves.^[141] e) STM image of in situ-cleaved $\text{Bi}_4\text{Rh}_3\text{I}_9$, $V = -0.1 \text{ V}$, $I = 240 \text{ pA}$, 300 K. f) Scanning tunneling potentiometry image of the same area as (e) with indicated direction of applied current, $I = 1.2 \text{ mA}$, distance of current carrying tips along vertical direction: $7.5 \mu\text{m}$, 300 K. Part (d) adapted with permission.^[141] Copyright 2016, American Chemical Society.

is corroborated by DFT calculations of bulk $\text{Bi}_4\text{Rh}_3\text{I}_9$ (Figure 8d, bottom, orange curve) showing E_F within the bandgap. Additional calculations of a thin film revealed that the surface is strongly n-doped (Figure 8d, yellow curve) with the bandgap at similar energies as found in the STS data (Figure 8d, top, red curve).^[141] This is in line with the strong 2D conductivity found by four-tip STM. The bandgap favorably moves quickly toward its bulk position already for the subsurface layer (Figure 8d, pink curve). To explain the surface n-doping, one has to consider the charging of the individual layers. It turns out that the 2DTI layer $(\text{Bi}_4\text{Rh})_3\text{I}$ transfers about one electron per unit cell to each of its neighboring spacer layers Bi_2I_8 such that it is positively charged by about two electrons per unit cell in equilibrium. Under these circumstances, E_F is in the bandgap of the 2DTI layer. At the surface, however, one neighboring spacer layer is missing, such that about one electron per unit cell remains on the 2DTI layer making it strongly n-doped.^[141] In principle, this could be counteracted by adding acceptors such as iodine onto the surface, but a relatively large amount of about one iodine atom per unit cell is required.^[142]

Using the four-tip STM, we also conducted scanning tunneling potentiometry.^[143] This method measures the tip voltage V that is required to nullify the current between tip and sample. Consequently, it maps the local potential, typically while current is flowing laterally. With four-tip STM, two tips can be used to inject the current, while a third tip is scanned in between to probe

the nullifying voltage.^[138,144] Consequently, the current induced potential is mapped. Figure 8e shows an area of the surface with 2DTI only, i.e., the islands exhibit step edges with height of a combined 2DTI and spacer layer. The potentiometry data show a barely visible overall decrease in the potential from the bottom to the top by about 0.1 mV due to the transport resistance. Much stronger features appear at the step edges and as patches on the surface of the 2DTI layers. They are identically present without applying current and are, hence, a static feature of the surface. Such features are caused by thermovoltage V_{thermo} resulting from a temperature difference of tip and sample $\Delta T \approx 1 \text{ K}$ and, as such, indicate spatially different slopes of the LDOS at E_F according to $V_{\text{thermo}} \propto \frac{d \ln(\text{LDOS}(E))}{dE} \Big|_{E_F}$.^[145,146] As a result, the method reveals fluctuations of LDOS(E_F) on the 2DTI terraces and a significant difference between step edges and terraces. The experiment did not provide any indication of preferred transport along the step edges in agreement with the observation that the topological edge states are not at E_F .

Other weak 3DTIs have been found,^[59,60,147,148] but none with E_F in the topological bandgap. Some uncertainty remains for ZrTe_5 , that is very close to a topological phase transition such that details on strain and temperature change the topological properties partly also in a favorable way.^[149] More interestingly, bismuthene, a honeycomb Bi monolayer on $\text{SiC}(0001)$, is a 2DTI that can be prepared in UHV with E_F inside the topological bandgap of size $\approx 1 \text{ eV}$.^[63] Here, preferential transport along step

edges might be detected by four-tip scanning tunneling potentiometry. Also, the ideal conductance of the edge state could be probed. It would lead to a potential drop that only appears at the end of the step edge, i.e., at the transition to the terrace in current direction.^[150]

7. Conclusions

In this article, we summarized some of the key contributions of surface science methods to the development of 3DTIs. Most importantly, ARPES could identify strong 3DTIs via the Dirac cone and its spin helicity of the TSS, whereas STS could identify weak 3DTIs via their helical edge states protected from backscattering at the dark surface. Moreover, ARPES was instrumental to monitor the tuning of the Dirac cone toward E_F , albeit the results are not compatible yet with the results from electric transport likely due to different treatments of the surfaces. Complementary, STS can map the potential disorder, most precisely via Landau level spectroscopy, and, hence, can monitor efforts to improve sample homogeneity. We have also shown exemplarily that particularly interesting materials can be identified as topological. In detail, we have discovered the first dual 3DTI Bi_1Te_1 and strong 3DTI properties in PCMs as an example material used in commercial applications. Two-photon ARPES was crucial to find the Dirac cone in these materials that only appeared in the unoccupied states due to strong p-doping. Finally, we have introduced the abilities of four-tip STM that can provide electric transport data in UHV without the requirement of ex situ contacting. We anticipate that this method will be perspective important to adapt the results from ARPES and STS to electric transport and, hence, to devices, as different surface treatments, that lead, e.g., to contaminations due to lithography, can be avoided.

Acknowledgements

We strongly appreciate the previous contributions to the publications reviewed in this manuscript by P. Bhaskar, S. Blügel, S. Borisenko, J.E. Boschker, V. Bragaglia, R. Callarco, S. Checchi, N. Demarina, V.L. Deringer, S. Döring, R. Dronskowski, Th. Fauster, M. Gehlmann, A. Georgi, E. Goliás, P. Gospodaric, M. Grob, D. Grützmacher, A. Guissani, C. Holl, B. Holländer, J. Kampmeier, B. Kaufmann, K. Koepf, P. Küppers, M. Lanius, M. Luysberg, E. Mlynczak, E. Neumann, C. Niu, O. Rader, J. Sanchez-Barriga, T. Schäpers, C.M. Schneider, M.R. Scholz, P. Schüffelgen, D. Subramaniam, J. van den Brink, A. Varykhalov, R. N. Wang, and C. Weyrich. M. Richter likes to thank U. Nietzsche for technical assistance. We, moreover, gratefully acknowledge funding by the Deutsche Forschungsgemeinschaft (DFG, German Research Foundation) via the project Mo 858/13-2 within the priority programme SPP1666 “Topological Insulators” and via the Strategy Clusters of Excellence “Matter and Light for Quantum Computing (ML4Q)” EXC 2004/1 390534769 as well as “Complexity and Topology in Quantum Matter (ct.qmat)” EXC 2147, project-id 39085-490. Open access funding enabled and organized by Projekt DEAL.

Conflict of Interest

The authors declare no conflict of interest.

Keywords

angular-resolved photoelectron spectroscopy, scanning tunneling spectroscopy, spin-polarized topological insulators

Received: January 29, 2020

Revised: April 3, 2020

Published online: May 12, 2020

- [1] D. J. Thouless, M. Kohmoto, M. P. Nightingale, M. den Nijs, *Phys. Rev. Lett.* **1982**, 49, 405.
- [2] Q. Niu, D. J. Thouless, Y. S. Wu, *Phys. Rev. B* **1985**, 31, 3372.
- [3] A. Cho, *Science* **2016**, 354, 21.
- [4] M. den Nijs, *Science* **2019**, 364, 835.
- [5] M. König, S. Wiedmann, C. Brune, A. Roth, H. Buhmann, L. W. Molenkamp, X. L. Qi, S. C. Zhang, *Science* **2007**, 318, 766.
- [6] M. Z. Hasan, C. L. Kane, *Rev. Mod. Phys.* **2010**, 82, 3045.
- [7] X. L. Qi, S. C. Zhang, *Rev. Mod. Phys.* **2011**, 83, 1057.
- [8] Y. Ando, *J. Phys. Soc. Jpn.* **2013**, 82, 102001.
- [9] B. Bahari, A. Ndao, F. Vallini, A. E. Amili, Y. Fainman, B. Kanté, *Science* **2017**, 358, 636.
- [10] J. Cha, K. W. Kim, C. Daraio, *Nature* **2018**, 564, 229.
- [11] Y. Yang, Z. Gao, H. Xue, L. Zhang, M. He, Z. Yang, R. Singh, Y. Chong, B. Zhang, H. Chen, *Nature* **2019**, 565, 622.
- [12] J. Ningyuan, C. Owens, A. Sommer, D. Schuster, J. Simon, *Phys. Rev. X* **2015**, 5, 021031.
- [13] X. Zhang, J. Wang, S. C. Zhang, *Phys. Rev. B* **2010**, 82, 245107.
- [14] L. He, X. Kou, K. L. Wang, *Phys. Status Solidi RRL* **2013**, 7, 50.
- [15] J. Han, A. Richardella, S. A. Siddiqui, J. Finley, N. Samarth, L. Liu, *Phys. Rev. Lett.* **2017**, 119, 077702.
- [16] J. Alicea, *Rep. Prog. Phys.* **2012**, 75, 076501.
- [17] S. D. Sarma, M. Freedman, C. Nayak, *NPJ Quantum Inf.* **2015**, 1, 15001.
- [18] J. Alicea, P. Fendley, *Annu. Rev. Condens. Matter Phys.* **2016**, 7, 119.
- [19] V. Lahtinen, J. Pachos, *SciPost Phys.* **2017**, 3, 021.
- [20] T. Zhang, Y. Jiang, Z. Song, H. Huang, Y. He, Z. Fang, H. Weng, C. Fang, *Nature* **2019**, 566, 475.
- [21] M. G. Vergniory, L. Elcoro, C. Felser, N. Regnault, B. A. Bernevig, Z. Wang, *Nature* **2019**, 566, 480.
- [22] F. Tang, H. C. Po, A. Vishwanath, X. Wan, *Nature* **2019**, 566, 486.
- [23] J. E. Moore, L. Balents, *Phys. Rev. B* **2007**, 75, 121306.
- [24] L. Fu, C. L. Kane, E. J. Mele, *Phys. Rev. Lett.* **2007**, 98, 106803.
- [25] L. Fu, C. L. Kane, *Phys. Rev. B* **2007**, 76, 045302.
- [26] C. L. Kane, E. J. Mele, *Phys. Rev. Lett.* **2005**, 95, 146802.
- [27] A. P. Schnyder, S. Ryu, A. Furusaki, A. W. W. Ludwig, *Phys. Rev. B* **2008**, 78, 195125.
- [28] S. Ryu, A. P. Schnyder, A. Furusaki, A. W. W. Ludwig, *New J. Phys.* **2009**, 12, 065010.
- [29] R. J. Slager, A. Mesaros, V. Juricic, J. Zanen, *Nat. Phys.* **2012**, 9, 98.
- [30] J. Kruthoff, J. de Boer, J. van Wezel, C. L. Kane, R. J. Slager, *Phys. Rev. X* **2017**, 7, 041069.
- [31] N. Mardirossian, M. Head-Gordon, *Mol. Phys.* **2017**, 115, 2315.
- [32] M. Stöhr, T. V. Voorhis, A. Tkatchenko, *Chem. Soc. Rev.* **2019**, 48, 4118.
- [33] D. Hsieh, D. Qian, L. Wray, Y. Xia, Y. S. Hor, R. J. Cava, M. Z. Hasan, *Nature* **2008**, 452, 970.
- [34] D. Hsieh, Y. Xia, L. Wray, D. Qian, A. Pal, J. H. Dil, J. Osterwalder, F. Meier, G. Bihlmayer, C. L. Kane, Y. S. Hor, R. J. Cava, M. Z. Hasan, *Science* **2009**, 323, 919.
- [35] H. Zhang, C. X. Liu, X. L. Qi, X. Dai, Z. Fang, S. C. Zhang, *Nat. Phys.* **2009**, 5, 438.
- [36] D. Hsieh, Y. Xia, D. Qian, L. Wray, J. H. Dil, F. Meier, J. Osterwalder, L. Patthey, J. G. Checkelsky, N. P. Ong, A. V. Fedorov, H. Lin,

- A. Bansil, D. Grauer, Y. S. Hor, R. J. Cava, M. Z. Hasan, *Nature* **2009**, 460, 1101.
- [37] D. Culcer, *Physica E* **2012**, 44, 860.
- [38] B. Yan, D. Zhang, C. Felser, *Phys. Status Solidi RRL* **2012**, 7, 148.
- [39] P. Cheng, C. Song, T. Zhang, Y. Zhang, Y. Wang, J. F. Jia, J. Wang, Y. Wang, B. F. Zhu, X. Chen, X. Ma, K. He, L. Wang, X. Dai, Z. Fang, X. Xie, X. L. Qi, C. X. Liu, S. C. Zhang, Q. K. Xue, *Phys. Rev. Lett.* **2010**, 105, 076801.
- [40] T. R. Devidas, E. P. Amaladass, S. Sharma, R. Rajaraman, D. Sornadurai, N. Subramanian, A. Mani, C. S. Sundar, A. Bharathi, *Europhys. Lett.* **2014**, 108, 67008.
- [41] M. Bianchi, D. Guan, S. Bao, J. Mi, B. B. Iversen, P. D. King, P. Hofmann, *Nat. Commun.* **2010**, 1, 128.
- [42] P. D. C. King, R. C. Hatch, M. Bianchi, R. Ovsyannikov, C. Lupulescu, G. Landolt, B. Slomski, J. H. Dil, D. Guan, J. L. Mi, E. D. L. Rienks, J. Fink, A. Lindblad, S. Svensson, S. Bao, G. Balakrishnan, B. B. Iversen, J. Osterwalder, W. Eberhardt, F. Baumberger, P. Hofmann, *Phys. Rev. Lett.* **2011**, 107, 096802.
- [43] E. Frantzeskakis, S. Ramankutty, N. de Jong, Y. Huang, Y. Pan, A. Tytarenko, M. Radovic, N. Plumb, M. Shi, A. Varykhalov, A. de Visser, E. van Heumen, M. Golden, *Phys. Rev. X* **2017**, 7, 041041.
- [44] B. Skinner, T. Chen, B. I. Shklovskii, *Phys. Rev. Lett.* **2012**, 109, 176801.
- [45] N. Borgwardt, J. Lux, I. Vergara, Z. Wang, A. A. Taskin, K. Segawa, P. H. M. van Loosdrecht, Y. Ando, A. Rosch, M. Grüninger, *Phys. Rev. B* **2016**, 93, 245149.
- [46] M. Morgenstern, C. Wittneven, R. Dombrowski, R. Wiesendanger, *Phys. Rev. Lett.* **2000**, 84, 5588.
- [47] M. Morgenstern, J. Klijn, C. Meyer, M. Getzlaff, R. Adelung, R. A. Römer, K. Rossnagel, L. Kipp, M. Skibowski, R. Wiesendanger, *Phys. Rev. Lett.* **2002**, 89, 136806.
- [48] H. Beidenkopf, P. Roushan, J. Seo, L. Gorman, I. Drozdov, Y. S. Hor, R. J. Cava, A. Yazdani, *Nat. Phys.* **2011**, 7, 939.
- [49] J. Dai, D. West, X. Wang, Y. Wang, D. Kwok, S. W. Cheong, S. Zhang, W. Wu, *Phys. Rev. Lett.* **2016**, 117, 106401.
- [50] J. Kellner, G. Bihlmayer, V. L. Deringer, M. Liebmann, C. Pauly, A. Giussani, J. E. Boschker, R. Calarco, R. Dronskowski, M. Morgenstern, *Phys. Rev. B* **2017**, 96, 245408.
- [51] T. Hanaguri, K. Igarashi, M. Kawamura, H. Takagi, T. Sasagawa, *Phys. Rev. B* **2010**, 82, 081305.
- [52] Y. S. Fu, M. Kawamura, K. Igarashi, H. Takagi, T. Hanaguri, T. Sasagawa, *Nat. Phys.* **2014**, 10, 815.
- [53] Y. Okada, Y. Zhou, C. Dhitai, D. Walkup, Y. Ran, Z. Wang, S. D. Wilson, V. Madhavan, *Phys. Rev. Lett.* **2012**, 109, 166407.
- [54] C. Pauly, C. Saunus, M. Liebmann, M. Morgenstern, *Phys. Rev. B* **2015**, 92, 085140.
- [55] A. Takayama, T. Sato, S. Souma, T. Oguchi, T. Takahashi, *Phys. Rev. Lett.* **2015**, 114, 066402.
- [56] M. Bianchi, F. Song, S. Coool, Å. F. Monsen, E. Wahlström, J. A. Miwa, E. D. L. Rienks, D. A. Evans, A. Strozicka, J. I. Pascual, M. Leandersson, T. Balasubramanian, P. Hofmann, J. W. Wells, *Phys. Rev. B* **2015**, 91, 165307.
- [57] I. K. Drozdov, A. Alexandradinata, S. Jeon, S. Nadj-Perge, H. Ji, R. J. Cava, B. A. Bernevig, A. Yazdani, *Nat. Phys.* **2014**, 10, 664.
- [58] C. Pauly, B. Rasche, K. Koepf, M. Liebmann, M. Pratzner, M. Richter, J. Kellner, M. Eschbach, B. Kaufmann, L. Plucinski, C. M. Schneider, M. Ruck, J. van den Brink, M. Morgenstern, *Nat. Phys.* **2015**, 11, 338.
- [59] X. B. Li, W. K. Huang, Y. Y. Lv, K. W. Zhang, C. L. Yang, B. B. Zhang, Y. Chen, S. H. Yao, J. Zhou, M. H. Lu, L. Sheng, S. C. Li, J. F. Jia, Q. K. Xue, Y. F. Chen, D. Y. Xing, *Phys. Rev. Lett.* **2016**, 116, 176803.
- [60] R. Wu, J. Z. Ma, S. M. Nie, L. X. Zhao, X. Huang, J. X. Yin, B. B. Fu, P. Richard, G. F. Chen, Z. Fang, X. Dai, H. M. Weng, T. Qian, H. Ding, S. Pan, *Phys. Rev. X* **2016**, 6, 021017.
- [61] P. Sessi, D. D. Sante, A. Szczerbakow, F. Glott, S. Wilfert, H. Schmidt, T. Bathon, P. Dziawa, M. Greiter, T. Neupert, G. Sangiovanni, T. Story, R. Thomale, M. Bode, *Science* **2016**, 354, 1269.
- [62] L. Peng, Y. Yuan, G. Li, X. Yang, J. J. Xian, C. J. Yi, Y. G. Shi, Y. S. Fu, *Nat. Commun.* **2017**, 8, 659.
- [63] F. Reis, G. Li, L. Dudy, M. Bauernfeind, S. Glass, W. Hanke, R. Thomale, J. Schäfer, R. Claessen, *Science* **2017**, 357, 287.
- [64] C. Meyer, J. Klijn, M. Morgenstern, R. Wiesendanger, *Phys. Rev. Lett.* **2003**, 91, 076803.
- [65] S. H. Kim, K. H. Jin, J. Park, J. S. Kim, S. H. Jhi, H. W. Yeom, *Sci. Rep.* **2016**, 6, 33193.
- [66] A. Bansil, H. Lin, T. Das, *Rev. Mod. Phys.* **2016**, 88, 021004.
- [67] B. Lampert, K. Reichelt, *J. Cryst. Growth* **1981**, 51, 203.
- [68] D. Teweldebrhan, V. Goyal, A. A. Balandin, *Nano Lett.* **2010**, 10, 1209.
- [69] Y. Xia, D. Qian, D. Hsieh, L. Wray, A. Pal, H. Lin, A. Bansil, D. Grauer, Y. S. Hor, R. J. Cava, M. Z. Hasan, *Nat. Phys.* **2009**, 5, 398.
- [70] D. Hsieh, Y. Xia, D. Qian, L. Wray, F. Meier, J. H. Dil, J. Osterwalder, L. Patthey, A. V. Fedorov, H. Lin, A. Bansil, D. Grauer, Y. S. Hor, R. J. Cava, M. Z. Hasan, *Phys. Rev. Lett.* **2009**, 103, 146401.
- [71] C. Seibel, H. Maaß, H. Bentmann, J. Braun, K. Sakamoto, M. Arita, K. Shimada, J. Minár, H. Ebert, F. Reinert, *J. Electr. Spectrosc. Relat. Phenom.* **2015**, 201, 110.
- [72] C. Pauly, G. Bihlmayer, M. Liebmann, M. Grob, A. Georgi, D. Subramaniam, M. R. Scholz, J. Sánchez-Barriga, A. Varykhalov, S. Blügel, O. Rader, M. Morgenstern, *Phys. Rev. B* **2012**, 86, 235106.
- [73] G. Wang, X. Zhu, J. Wen, X. Chen, K. He, L. Wang, X. Ma, Y. Liu, X. Dai, Z. Fang, J. Jia, Q. Xue, *Nano Res.* **2010**, 3, 874.
- [74] Y. Jiang, Y. Y. Sun, M. Chen, Y. Wang, Z. Li, C. Song, K. He, L. Wang, X. Chen, Q. K. Xue, X. Ma, S. B. Zhang, *Phys. Rev. Lett.* **2012**, 108, 066809.
- [75] K. Hofer, C. Becker, D. Rata, J. Swanson, P. Thalmeier, L. H. Tjeng, *Proc. Nat. Acad. Sci.* **2014**, 111, 14979.
- [76] S. Souma, K. Kosaka, T. Sato, M. Komatsu, A. Takayama, T. Takahashi, M. Kriener, K. Segawa, Y. Ando, *Phys. Rev. Lett.* **2011**, 106, 216803.
- [77] S. Hüfner, *Photoelectron Spectroscopy*, Springer, Berlin Heidelberg **1995**.
- [78] H. Ebert, D. Ködderitzsch, J. Minár, *Rep. Prog. Phys.* **2011**, 74, 096501.
- [79] C. Jozwiak, C. H. Park, K. Gottlieb, C. Hwang, D. H. Lee, S. G. Louie, J. D. Denlinger, C. R. Rotundu, R. J. Birgeneau, Z. Hussain, A. Lanzara, *Nat. Phys.* **2013**, 9, 293.
- [80] K. Medjanik, O. Fedchenko, S. Chernov, D. Kutnyakhov, M. Ellguth, A. Oelsner, B. Schönhense, T. R. F. Peixoto, P. Lutz, C. H. Min, F. Reinert, S. Däster, Y. Acremann, J. Viehhaus, W. Wurth, H. J. Elmers, G. Schönhense, *Nat. Mater.* **2017**, 16, 615.
- [81] Z. Ren, A. A. Taskin, S. Sasaki, K. Segawa, Y. Ando, *Phys. Rev. B* **2010**, 82, 241306.
- [82] D. Kong, Y. Chen, J. J. Cha, Q. Zhang, J. G. Analytis, K. Lai, Z. Liu, S. S. Hong, K. J. Koski, S. K. Mo, Z. Hussain, I. R. Fisher, Z. X. Shen, Y. Cui, *Nat. Nanotechnol.* **2011**, 6, 705.
- [83] Y. Xu, I. Miotkowski, C. Liu, J. Tian, H. Nam, N. Alidoust, J. Hu, C. K. Shih, M. Z. Hasan, Y. P. Chen, *Nat. Phys.* **2014**, 10, 956.
- [84] Y. Xu, I. Miotkowski, Y. P. Chen, *Nat. Commun.* **2016**, 7, 11434.
- [85] J. Zhang, C. Z. Chang, Z. Zhang, J. Wen, X. Feng, K. Li, M. Liu, K. He, L. Wang, X. Chen, Q. K. Xue, X. Ma, Y. Wang, *Nat. Commun.* **2011**, 2, 574.
- [86] J. D. Sau, R. M. Lutchyn, S. Tewari, S. D. Sarma, *Phys. Rev. B* **2010**, 82, 094522.
- [87] A. L. Rakhmanov, A. V. Rozhkov, F. Nori, *Phys. Rev. B* **2011**, 84, 075141.
- [88] J. P. Xu, C. Liu, M. X. Wang, J. Ge, Z. L. Liu, X. Yang, Y. Chen, Y. Liu, Z. A. Xu, C. L. Gao, D. Qian, F. C. Zhang, J. F. Jia, *Phys. Rev. Lett.* **2014**, 112, 217001.

- [89] J. Kellner, M. Eschbach, J. Kampmeier, M. Lanius, E. Młyńczak, G. Mussler, B. Holländer, L. Plucinski, M. Liebmann, D. Grützmacher, C. M. Schneider, M. Morgenstern, *Appl. Phys. Lett.* **2015**, 107, 251603.
- [90] C. Weyrich, M. Drögeler, J. Kampmeier, M. Eschbach, G. Mussler, T. Merzenich, T. Stoica, I. E. Batov, J. Schubert, L. Plucinski, B. Beschoten, C. M. Schneider, C. Stampfer, D. Grützmacher, T. Schäpers, *J. Phys.: Condens. Matter* **2016**, 28, 495501.
- [91] M. Eschbach, E. Młyńczak, J. Kellner, J. Kampmeier, M. Lanius, E. Neumann, C. Weyrich, M. Gehlmann, P. Gospodarič, S. Döring, G. Mussler, N. Demarina, M. Luysberg, G. Bihlmayer, T. Schäpers, L. Plucinski, S. Blügel, M. Morgenstern, C. M. Schneider, D. Grützmacher, *Nat. Commun.* **2015**, 6, 8816.
- [92] J. Wang, X. Chen, B. F. Zhu, S. C. Zhang, *Phys. Rev. B* **2012**, 85, 235131.
- [93] Y. Tanaka, Z. Ren, T. Sato, K. Nakayama, S. Souma, T. Takahashi, K. Segawa, Y. Ando, *Nat. Phys.* **2012**, 8, 800.
- [94] P. Dziawa, B. J. Kowalski, K. Dybko, R. Buczko, A. Szczerbakow, M. Szołt, E. Łlusakowska, T. Balasubramanian, B. M. Wojek, M. H. Berntsen, O. Tjernberg, T. Story, *Nat. Mater.* **2012**, 11, 1023.
- [95] Z. K. Liu, B. Zhou, Y. Zhang, Z. J. Wang, H. M. Weng, D. Prabhakaran, S. K. Mo, Z. X. Shen, Z. Fang, X. Dai, Z. Hussain, Y. L. Chen, *Science* **2014**, 343, 864.
- [96] Z. K. Liu, J. Jiang, B. Zhou, Z. J. Wang, Y. Zhang, H. M. Weng, D. Prabhakaran, S. K. Mo, H. Peng, P. Dudin, T. Kim, M. Hoesch, Z. Fang, X. Dai, Z. X. Shen, D. L. Feng, Z. Hussain, Y. L. Chen, *Nat. Mater.* **2014**, 13, 677.
- [97] M. Yan, H. Huang, K. Zhang, E. Wang, W. Yao, K. Deng, G. Wan, H. Zhang, M. Arita, H. Yang, Z. Sun, H. Yao, Y. Wu, S. Fan, W. Duan, S. Zhou, *Nat. Commun.* **2017**, 8, 257.
- [98] S. Y. Xu, I. Belopolski, N. Alidoust, M. Neupane, G. Bian, C. Zhang, R. Sankar, G. Chang, Z. Yuan, C. C. Lee, S. M. Huang, H. Zheng, J. Ma, D. S. Sanchez, B. Wang, A. Bansil, F. Chou, P. P. Shibayev, H. Lin, S. Jia, M. Z. Hasan, *Science* **2015**, 349, 613.
- [99] B. Lv, H. Weng, B. Fu, X. Wang, H. Miao, J. Ma, P. Richard, X. Huang, L. Zhao, G. Chen, Z. Fang, X. Dai, T. Qian, H. Ding, *Phys. Rev. X* **2015**, 5, 031013.
- [100] T. Rauch, M. Flieger, J. Henk, I. Mertig, A. Ernst, *Phys. Rev. Lett.* **2014**, 112, 016802.
- [101] L. Fu, *Phys. Rev. Lett.* **2011**, 106, 106802.
- [102] M. Eschbach, M. Lanius, C. Niu, E. Młyńczak, P. Gospodarič, J. Kellner, P. Schüffelgen, M. Gehlmann, S. Döring, E. Neumann, M. Luysberg, G. Mussler, L. Plucinski, M. Morgenstern, D. Grützmacher, G. Bihlmayer, S. Blügel, C. M. Schneider, *Nat. Commun.* **2017**, 8, 14976.
- [103] S. Murakami, *Phys. Rev. Lett.* **2006**, 97, 236805.
- [104] F. Yang, L. Miao, Z. F. Wang, M. Y. Yao, F. Zhu, Y. R. Song, M. X. Wang, J. P. Xu, A. V. Fedorov, Z. Sun, G. B. Zhang, C. Liu, F. Liu, D. Qian, C. L. Gao, J. F. Jia, *Phys. Rev. Lett.* **2012**, 109, 016801.
- [105] F. Xiong, A. D. Liao, D. Estrada, E. Pop, *Science* **2011**, 332, 568.
- [106] D. Loke, T. H. Lee, W. J. Wang, L. P. Shi, R. Zhao, Y. C. Yeo, T. C. Chong, S. R. Elliott, *Science* **2012**, 336, 1566.
- [107] M. Wuttig, S. Raoux, *Z. Anorg. Allg. Chem.* **2012**, 638, 2455.
- [108] M. Wuttig, N. Yamada, *Nat. Mater.* **2007**, 6, 824.
- [109] M. Liebmann, C. Rinaldi, D. D. Sante, J. Kellner, C. Pauly, R. N. Wang, J. E. Boschker, A. Giussani, S. Bertoli, M. Cantoni, L. Baldrati, M. Asa, I. Vobornik, G. Panaccione, D. Marchenko, J. Sánchez-Barriga, O. Rader, R. Calarco, S. Picozzi, R. Bertacco, M. Morgenstern, *Adv. Mater.* **2015**, 28, 560.
- [110] H. J. Elmers, R. Wallauer, M. Liebmann, J. Kellner, M. Morgenstern, R. N. Wang, J. E. Boschker, R. Calarco, J. Sánchez-Barriga, O. Rader, D. Kutnyakhov, S. V. Chernov, K. Medjanik, C. Tusche, M. Ellguth, H. Volfova, S. Borek, J. Braun, J. Minár, H. Ebert, G. Schönhense, *Phys. Rev. B* **2016**, 94, 201403.
- [111] J. Krempaský, H. Volfová, S. Muff, N. Pilet, G. Landolt, M. Radović, M. Shi, D. Kriegner, V. Holý, J. Braun, H. Ebert, F. Bisti, V. A. Rogalev, V. N. Strocov, G. Springholz, J. Minár, J. H. Dil, *Phys. Rev. B* **2016**, 94, 205111.
- [112] J. Kim, J. Kim, S. H. Jhi, *Phys. Rev. B* **2010**, 82, 201312.
- [113] S. V. Eremeev, G. Landolt, T. V. Menshchikova, B. Slomski, Y. M. Koroteev, Z. S. Aliev, M. B. Babanly, J. Henk, A. Ernst, L. Patthey, A. Eich, A. A. Khajetoorians, J. Hagemeyer, O. Pietzsch, J. Wiebe, R. Wiesendanger, P. M. Echenique, S. S. Tsirkin, I. R. Amiraslanov, J. H. Dil, E. V. Chulkov, *Nat. Commun.* **2012**, 3, 635.
- [114] J. Kim, J. Kim, K. S. Kim, S. H. Jhi, *Phys. Rev. Lett.* **2012**, 109, 146601.
- [115] I. Silkin, Y. Koroteev, G. Bihlmayer, E. Chulkov, *Appl. Surf. Sci.* **2013**, 267, 169.
- [116] R. E. Simpson, P. Fons, A. V. Kolobov, T. Fukaya, M. Krbal, T. Yagi, J. Tominaga, *Nat. Nanotechnol.* **2011**, 6, 501.
- [117] J. Tominaga, A. V. Kolobov, P. Fons, T. Nakano, S. Murakami, *Adv. Mater. Interfaces* **2013**, 1, 1300027.
- [118] C. Pauly, M. Liebmann, A. Giussani, J. Kellner, S. Just, J. Sánchez-Barriga, E. Rienks, O. Rader, R. Calarco, G. Bihlmayer, M. Morgenstern, *Appl. Phys. Lett.* **2013**, 103, 243109.
- [119] J. Kellner, G. Bihlmayer, M. Liebmann, S. Otto, C. Pauly, J. E. Boschker, V. Bragaglia, S. Cecchi, R. N. Wang, V. L. Deringer, P. Küppers, P. Bhaskar, E. Golias, J. Sánchez-Barriga, R. Dronskowski, T. Fauster, O. Rader, R. Calarco, M. Morgenstern, *Commun. Phys.* **2018**, 1, 5.
- [120] H. Hayat, K. I. Kohary, C. D. Wright, in *Phase Change Memory*, Springer International Publishing (Ed: A. Pigozzo), Cham **2017**, p. 223.
- [121] T. Schäfer, P. M. Konze, J. D. Huyeng, V. L. Deringer, T. Lesieur, P. Müller, M. Morgenstern, R. Dronskowski, M. Wuttig, *Chem. Mater.* **2017**, 29, 6749.
- [122] S. V. Eremeev, T. V. Menshchikova, I. V. Silkin, M. G. Vergniory, P. M. Echenique, E. V. Chulkov, *Phys. Rev. B* **2015**, 91, 245145.
- [123] H. J. Zandvliet, A. van Houselt, *Annu. Rev. Anal. Chem.* **2009**, 2, 37.
- [124] J. Tersoff, D. R. Hamann, *Phys. Rev. B* **1985**, 31, 805.
- [125] M. Morgenstern, D. Haude, V. Gudmundsson, C. Wittneven, R. Dombrowski, C. Steinebach, R. Wiesendanger, *J. Electr. Spectrosc. Relat. Phenom.* **2000**, 109, 127.
- [126] M. Morgenstern, *Surf. Rev. Lett.* **2003**, 10, 933.
- [127] M. Wuttig, D. Lüsebrink, D. Wamwangi, W. Wełnic, M. Gilleßen, R. Dronskowski, *Nat. Mater.* **2006**, 6, 122.
- [128] B. S. Lee, J. R. Abelson, S. G. Bishop, D. H. Kang, B. Ki Cheong, K. B. Kim, *J. Appl. Phys.* **2005**, 97, 093509.
- [129] K. S. Novoselov, A. K. Geim, S. V. Morozov, D. Jiang, M. I. Katsnelson, I. V. Grigorieva, S. V. Dubonos, A. A. Firsov, *Nature* **2005**, 438, 197.
- [130] A. H. C. Neto, F. Guinea, N. M. R. Peres, K. S. Novoselov, A. K. Geim, *Rev. Mod. Phys.* **2009**, 81, 109.
- [131] T. Champel, S. Florens, *Phys. Rev. B* **2010**, 82, 045421.
- [132] Z. Ringel, Y. E. Kraus, A. Stern, *Phys. Rev. B* **2012**, 86, 045102.
- [133] H. Obuse, S. Ryu, A. Furusaki, C. Mudry, *Phys. Rev. B* **2014**, 89, 155315.
- [134] Y. Yoshimura, A. Matsumoto, Y. Takane, K. I. Imura, *Phys. Rev. B* **2013**, 88, 045408.
- [135] B. Rasche, A. Isaeva, M. Ruck, S. Borisenko, V. Zabolotnyy, B. Büchner, K. Koepf, C. Ortix, M. Richter, J. van den Brink, *Nat. Mater.* **2013**, 12, 422.
- [136] B. Rasche, A. Isaeva, M. Ruck, K. Koepf, M. Richter, J. van den Brink, *Sci. Rep.* **2016**, 6, 20645.
- [137] S. Konschuh, M. Gmitra, J. Fabian, *Phys. Rev. B* **2010**, 82, 245412.

- [138] B. Voigtländer, V. Cherepanov, S. Korte, A. Leis, D. Cuma, S. Just, F. Lüpke, *Rev. Sci. Instrum.* **2018**, *89*, 101101.
- [139] S. Just, M. Blab, S. Korte, V. Cherepanov, H. Soltner, B. Voigtländer, *Phys. Rev. Lett.* **2015**, *115*, 066801.
- [140] S. Just, H. Soltner, S. Korte, V. Cherepanov, B. Voigtländer, *Phys. Rev. B* **2017**, *95*, 075310.
- [141] C. Pauly, B. Rasche, K. Koepf, M. Richter, S. Borisenko, M. Liebmann, M. Ruck, J. van den Brink, M. Morgenstern, *ACS Nano* **2016**, *10*, 3995.
- [142] M. P. Ghimire, M. Richter, *Nano Lett.* **2017**, *17*, 6303.
- [143] P. Murali, D. W. Pohl, *Appl. Phys. Lett.* **1986**, *48*, 514.
- [144] F. Lüpke, S. Korte, V. Cherepanov, B. Voigtländer, *Rev. Sci. Instrum.* **2015**, *86*, 123701.
- [145] J. A. Stovng, P. Lipavský, *Phys. Rev. B* **1990**, *42*, 9214.
- [146] T. Druga, M. Wenderoth, J. Homoth, M. A. Schneider, R. G. Ulbrich, *Rev. Sci. Instrum.* **2010**, *81*, 083704.
- [147] M. M. Hosen, K. Dimitri, A. K. Nandy, A. Aperis, R. Sankar, G. Dhakal, P. Maldonado, F. Kabir, C. Sims, F. Chou, D. Kaczorowski, T. Durakiewicz, P. M. Oppeneer, M. Neupane, *Nat. Commun.* **2018**, *9*, 3002.
- [148] R. Noguchi, T. Takahashi, K. Kuroda, M. Ochi, T. Shirasawa, M. Sakano, C. Bareille, M. Nakayama, M. D. Watson, K. Yaji, A. Harasawa, H. Iwasawa, P. Dudin, T. K. Kim, M. Hoesch, V. Kandyba, A. Giampietri, A. Barinov, S. Shin, R. Arita, T. Sasagawa, T. Kondo, *Nature* **2019**, *566*, 518.
- [149] Y. Zhang, C. Wang, L. Yu, G. Liu, A. Liang, J. Huang, S. Nie, X. Sun, Y. Zhang, B. Shen, J. Liu, H. Weng, L. Zhao, G. Chen, X. Jia, C. Hu, Y. Ding, W. Zhao, Q. Gao, C. Li, S. He, L. Zhao, F. Zhang, S. Zhang, F. Yang, Z. Wang, Q. Peng, X. Dai, Z. Fang, Z. Xu, et al., *Nat. Commun.* **2017**, *8*, 15512.
- [150] U. Klass, W. Dietsche, K. von Klitzing, K. Ploog, *Surf. Sci.* **1992**, *263*, 97.
- [151] A. L. Efros, B. I. Shklovskii, *J. Phys. C: Solid State Phys.* **1975**, *8*, L49.
- [152] F. Lüpke, S. Just, M. Eschbach, T. Heider, E. Młyńczak, M. Lanius, P. Schüffgen, D. Rosenbach, N. von den Driesch, V. Cherepanov, G. Mussler, L. Plucinski, D. Grützmaker, C. M. Schneider, F. S. Tautz, B. Voigtländer, *NPJ Quantum Mater.* **2018**, *3*, 46.
- [153] K. Koepf, H. Eschrig, *Phys. Rev. B* **1999**, *59*, 1743.